energies

MDPI

Article

Performance of a Direct-Driven Wave Energy Point Absorber with High Inertia Rotatory Power Take-off

Simon Thomas [1,*], Marianna Giassi [1], Malin Göteman [1], Martyn Hann [2], Edward Ransley [2], Jan Isberg [1] and Jens Engström [1]

[1] Lägerhyddsvägen 1, Division of Electricity, Angströmlaboratoriet, Uppsala University, 75237 Uppsala, Sweden; Marianna.Giassi@angstrom.uu.se (M.G.); Malin.Goteman@angstrom.uu.se (M.G.); Jan.Isberg@angstrom.uu.se (J.I.); Jens.Engstrom@angstrom.uu.se (J.E.)

[2] School of Engineering, University of Plymouth, Drake Circuit, Plymouth PL4 8AA, UK; Martyn.Hann@plymouth.ac.uk (M.H.); Edward.Ransley@plymouth.ac.uk (E.R.)

* Correspondence: simon.thomas@angstrom.uu.se

Received: 1 August 2018; Accepted: 30 August 2018; Published: 4 September 2018

Abstract: An alternating rotatory generator using an eddy current break is developed as a physical scale model of a direct-driven floating point absorber power take-off (PTO) for wave tank tests. It is shown that this design is a simple and cost-effective way to get an accurate linear damping PTO. The device shows some beneficial characteristics, making it an interesting option for full scale devices: For similar weights the inertia can be significantly higher than for linear generators, allowing it to operate with natural frequencies close to typical wave frequencies. The influence of the higher inertia on the power absorption is tested using both a numerical simulation and physical wave tank tests. With the increased inertia the PTO is able to absorb more than double the energy of a comparable direct-driven linear generator in some sea states. Moreover, the alternating rotatory generator allows the absorption characteristic to be tuned by changing the inertia and the generator damping.

Keywords: wave energy; power take-off; direct-driven; wave tank test; physical scale model; natural frequency tuning; floating point absorber

1. Introduction

Physical wave tank tests play an important role in validating numerical results and testing devices under realistic and repeatable conditions. They are an important, while cost efficient, step in the development of a wave energy converter (WEC) before going to full scale. In this paper a new power take-off (PTO) design for floating point absorbers is presented which has been developed especially for wave tank tests.

Despite extensive research on wave energy during the last decades [1], the levelized cost of energy is too high compared to other energy sources [2]. One way of lowering these costs is to simplify the mechanical design of the wave energy converter, and here especially the power take off (PTO) [3]. One notable WEC design, which was also the inspiration for the WEC presented here, is the floating point absorber with linear generator, for example developed at Uppsala University [4] (UU-WEC), CorPower [5] or the Archimedes Wave Swing [6]. A disadvantage of most of these devices, is the high natural frequency, leading to a poor capture width for sea states with long wave energy periods, if no additional control [7] or similar mechanism [8,9] is applied.

A simple way to increase the natural frequency occurred while developing a power take-off device (PTO) mimicking an ideal generator for model scale wave tank tests of WEC arrays. Existing physical scale models of WECs can roughly be divided into two groups: Simple and cost-effective models neglecting the generator force or replacing it with a constant friction [10], while advanced scale

models may use electric actuators mimicking the generator [11–14]. The latter may mimic the generator behaviour very well, but relays heavily on a good control system. For the purpose of working under time-constraints with several physical scale WECs, a motor-based approach, seemed too complex and too susceptible to faults. But on the same side, when concentrating on the absorbed power a high accurate generator model is indispensable.

The physical model presented here combines the simplicity and cost-efficiency of inaccurate models, whilst providing a nearly ideal damping force and an improved power absorption. This is done by combining two fundamental concepts used for PTOs: The alternating linear generator and the unidirectional rotatory generator. Using rotatory generators for wave power requires a gearbox (hydraulic, pneumatic [15] or mechanical [16,17]), transforming the linear alternating motion of the wave into a unidirectional rotatory motion. Direct-driven linear generators on the other hand generate the electric energy directly from the alternating motion without the losses of a gearbox, but require a rectifier for grid integration [15]. For the physical model presented here, a direct-driven alternating rotatory PTO is used, that does not require a complex gearbox and has a much higher inertia than direct-driven linear generators or unidirectional rotatory generator. Direct-driven rotatory generators converters for low speeds, but with unidirectional motion, play already a significant role in wind power [18,19] and were also tested for WECs [16]. Bi-directional direct-driven rotary converts however can be hardly found [20,21]. In this paper the characteristics of such a PTO, and especially the influence of the high inertia, compared to a direct-driven linear generator will be investigated. A similar analysis of the influence of the inertia on the absorbed power, but for a cylindrical bottom-hinged WEC was performed in [22], while the effects in resonance frequency between fixed and self referenced point absorber are discussed in [23].

PTO concepts using rotational electrical generators have been considered previously by a number of developers:

- An innovative approach using a rotatory generator for wave energy and tuning the natural frequency is discussed in [9], where a pendulum excited by the heave motion of the WEC turns a rotatory generator. The pendulum can be designed, so that it is in resonance at the frequency of the incident wave and so the power absorption is maximised.
- The dynamo presented in [16] converts the bi-directional movement of the buoy into a unidirectional rotation for the generator what might result in similar inertia effects as the PTO presented here. However, the design requires a complex gearbox and a rectifier to make the pulsed output of the WEC grid conforming. The effects of the increased inertia on the power absorption are not investigated.
- Concepts based on flywheels, like in [17] (and similarly in [24,25]) convert the linear bi-directional motion of the buoy into a bi-directional rotation, but the generator connected to a flywheel is run in uni-directional motion. A controllable clutch connects the generator with the buoy shaft whenever it might accelerate the generator shaft. In the meantime the generator is run by the energy stored in the flywheel. As the generator's angular velocity does not follow the buoy's velocity, it does not show the high inertia of the alternating generator and is only able to absorb energy while the buoy is moving downwards. The power output is very smooth and may need no or only little smoothing to be grid compatible, and so the peak-to-average power ratio is much lower than in conventional WEC designs.
- A bi-directional winch based design, similar to the concept presented here, but with a gearbox and the PTO placed in the buoy is used in the WEC described in [21]. The generator is a conventional electrical machine used in industrial servo applications. It only produces power while moving upwards and operates in motoring mode during downwards motion.

In this paper a numerical simulation and wave tank experiments were used to characterise the system. The numerical time-domain model uses linear potential flow theory to calculate the absorbed power of floating point absorber with ideal generator for different inertiae and damping coefficients.

The physical model is characterised with experiments in the Ocean Basin in the COAST Laboratory at the University of Plymouth are conducted to test the influence of the inertia in different sea states.

In the following section the scale PTO model will be presented, showing its characteristics in comparison to a linear generator PTO. Theoretical background on wave body interactions, used for the numerical simulation, is given in Section 3. In Section 4 the physical and in Section 5 the numerical test set-up are presented, the results and their discussion can be found in Section 6, before the conclusions are drawn in Section 7. Unless otherwise stated, all values in this paper refer to a full scale device, values obtained from the scale model are presented as full scale values using Froude scaling.

2. Design of the Physical Model PTO

The most important goal during the design of the physical scale PTO was a linear behaviour to ease the comparison of theoretical and practical results. High friction is often a problem in scale model tests and therefore it is necessary to aim for a low friction design. For the design of the PTO the issue is addressed by using a rotational generator, assuming that a low friction rotation bearing can be easier achieved than an equivalent translational bearing. Furthermore, having a rotational design, all deviations will reappear after each turn, what simplifies the identification, and the stroke length, which can influence the power absorption significantly [26], can easily be extended. For hassle free utilisation in wave tank tests, the PTO should be easy to install and operate and, regarding array tests, cost-efficient and easy to replicate. This is achieved by using mostly standard parts.

To get an accurate and cost-effective speed-proportional damping, different principles are examined:

- Viscous dampers create an accurate damping force by forcing a fluid through a small hole. The damping can be changed by varying the hole diameter.
- Eddy-current breaks provide a nearly ideal, contactless velocity proportional force by moving a conductive material through a magnetic field. The damping can be adjusted by varying the magnetic field.
- Small permanent electric generators, like automotive alternators or bicycle hub dynamos are cost effective and provide the absorbed power directly.

We choose the eddy current break, as it is, despite its simplicity, the most accurate principle and has been successfully used in scale models [27,28]. Viscous dampers were occasionally used to simulate PTO forces [29], but their damping depends on the temperature, as the viscosity of most fluids changes significantly with the temperature, so monitoring the temperature is necessary for accurate results. Using a real generator comes with the advantage, that the absorbed power can be measured directly, rather than be calculated from the velocity. On the other hand, the characteristics of bicycle dynamos or car alternators differs from the three phase synchronous generator used in many direct-driven full scale WECs; static and dynamic friction, cogging forces, hysteresis, saturation are individual parameters of a generator; for general research it is beneficial to use an ideal linear generator instead.

The final set-up developed consists of a bicycle wheel truing stand (Tacx T3175) screwed on a table; see the generalized sketch in Figure 1 and the a photo and sketch of the device in the wave tank test in Figure 6 later in this paper. It is holding a bicycle front hub with disc break mounting holes (Shimano XT HB-M756). The bicycle hub has a low friction ball bearing. Instead of a disc break, a 2 mm thick aluminium disc with 40 mm diameter is mounted. A vice (Clarke CSV4E 100 mm) is located on the table below the disc, the edge of the aluminium (AL1050) is positioned between its clamps. The movable clamp holds a set of magnets (5× Neodymium N42 20 × 20 × 10). Changing the gap between the clamps changes the magnetic flux through the disc and so the PTO damping d_{PTO}. An estimation of the magnetic flux in dependence of the air gap length z is given in Equation (1),

$$B = B_r/\pi \left[\arctan\left(\frac{LW}{2z\sqrt{4z^2 + L^2 + W^2}} \right) - \arctan\left(\frac{LW}{2(D+z)\sqrt{4(D+z)^2 + L^2 + W^2}} \right) \right] \quad (1)$$

with L, W and D being the length, width and thickness of the magnet and B_r its remanence field.

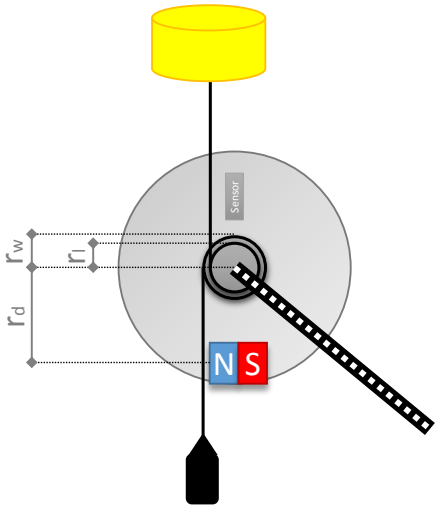

Figure 1. Simplified sketch of the PTO with relevant radii. Here r_d is the distance from the disc's centre to the magnets, r_w is the radius of the winch for the line leading to the weight, and r_l is the radius of the winch of the line leading to the buoys.

On the hub two ropes are installed, one is connected to the line going up to the buoy acting a positive moment on the hub, the other rope is connected to a weight acting as a counter moment on the hub. To capture the PTO position and speed, an Inertia Measurement Unit (IMU) based on the Intel Curie platform is mounted on the disc at distance r_S from the centre, recording acceleration in two directions and rotational speed. A similar position measurement system was used in [30]. Knowing acceleration (a_x, a_y) and rotational speed (ω), the angle α of the disc can be calculated:

$$\alpha = \arctan\left(\frac{a_x - r_S\omega^2}{a_y - \dot{\omega}r_S}\right), \tag{2}$$

and so the power:

$$P = (\dot{\omega}r_s)^2 d_{PTO}\,. \tag{3}$$

A detailed overview over the processing done can be found in Figure 2.

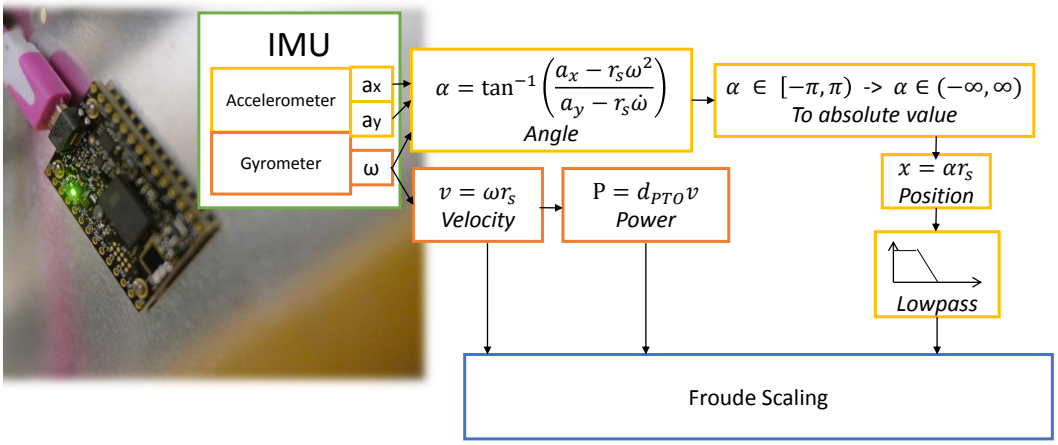

Figure 2. Processing of the measured data. Here v is the linearised velocity and x the linearised position.

2.1. Characteristics

A direct-driven linear generator, as used in many floating point absorbers wave energy converters is described by a mass-damper system. The force in the line F_l can be calculated as:

$$F_l = -\dot{x}_w d - m_w \ddot{x}_w - m_w g \,, \tag{4}$$

with x_w being the position of the weight, m_w the mass of the weight, d the overall damping and g the gravity acceleration.

The line force F_l of a rotational electric generator as described above can be expressed as:

$$F_l = (m_w r_w^2 / r_l + J/r_l)\ddot{\varphi} + (d_{PTO} r_d^2 / r_l)\dot{\varphi} + m_w g r_w / r_l \,, \tag{5}$$

with r_w being the radius the rope to the weight winds to the disc, r_l being the radius the line to the buoy winds on the disc, J is the moment of inertia of the rotor and g being acceleration. A sketch with all relevant radii can be found in Figure 1. Defining $x = r_l \varphi$ and $M = m_w (r_w / r_l)^2 + J/r_l^2$, we get:

$$F_l = M\ddot{x} + d_{PTO}(r_d / r_l)^2 \dot{x} + m_w g r_w / r_l \,, \tag{6}$$

where r_d is the distance between the centre of the disc and the magnets. Comparing Equation (4) with (6), the gearbox effect of the disc can be seen: The applied damping d_{PTO} is amplified by the ratio $(rd/r_l)^2$, thus for the 1:10 r_d/r_l ratio in the physical scale model the magnetic field can be 100 times weaker than for a linear generator. Unlike the linear generator the weight pulling downwards m_w and the inertia of the PTO M are not equal, latter includes also the disc inertia J/r_l^2. The inertia of a solid disc is:

$$J = 0.5 r_c^4 \pi \rho_c h_c \,, \tag{7}$$

with r_c being the radius of the disc, ρ_c being its density and h_c its thickness. By changing the ratio r_c^4/r_l, the disc can be designed to fit a specific inertia target.

2.2. Influence of Inertia on Absorbed Power

For simplification we assume the WEC to be a one body system with one degree of freedom (heave direction), assuming a stiff connection between buoy and the moving part of the PTO. In the presence of a flat water surface the system can be seen as an harmonic oscillator with the damped frequency:

$$\omega_d = \sqrt{k/M_t - (0.5d/M_t)^2} \,, \tag{8}$$

where k is the hydrostatic buoyancy stiffness of the buoy, M_t the total mass of inertia, including the mass and added mass of the buoy, the mass of the weights, the mass of the lines and the weight of the disc. The damping coefficient d is the sum of the electrical damping coefficient of the PTO d_{PTO} and the hydrodynamical damping coefficient of the buoy. The optimal d depends on the sea state [7]. As d has only a small influence compared to the natural frequency it is assumed to be fixed. Doing so the absorbed energy is proportional to the angular frequency respective velocity, and so:

$$\hat{E} \sim \hat{F}/(j\omega M_t + d - jk/\omega). \tag{9}$$

From Equation (9) follows that the most energy is absorbed when

$$M_t = k/\omega^2. \tag{10}$$

Controlling a WEC so that Equation (10) is always fulfilled, called complex conjugate control, requires an adjustable inertia or spring (an example for such and device can be found in [5]), or a reactive

generator. In many cases it may be enough, if the WEC is designed so that we get close to the condition of Equation (10) for most sea states.

The hydrostatic buoyancy stiffness k depends on the shape of the buoy. For a cylindrical buoy with radius r, k is

$$k = r^2 \pi \rho g. \tag{11}$$

If we compare to a cylindrical buoy with a diameter of 5 m, which have been used by Uppsala University in the Lysekil project (UU-WEC) [31], k would be about 192.6 kN/m, according to Equation (10) the inertia should be around 48.15 t for the 3 s period and 102.5 t for the 12 s case. For most WECs with direct-driven linear generators the total moving mass is much less (about 10 tonnes for the mentioned UU-WEC), as a higher mass makes the system, especially the deployment, very expensive. Those devices can be controlled by changing the generator damping or by latching the translator (which can be seen as a extreme form of the former). Both, especially damping control, are not as efficient as complex-conjugate control.

With the generator presented in this paper, changing the mass is possible by changing r_m. Regarding the trend to simplify devices to cut costs and increase reliability, in wave climates where the region of high energy sea states is centred around one sea state, it might be sufficient, if the WEC is designed so that it fulfils Equation (10) only for this sea state.

Especially for direct-driven generators, changing the damped frequency of the system by changing the generator damping d_{PTO} is a cost effective way to adapt the WEC to different sea states [32], but not as effective as changing the natural frequency. However, to achieve the optimal power absorption, both the natural frequency and the damping have to match the sea state.

Buoy and generator are connected with a line, in case the line is loose, both bodies can move independently. In that case Equation (8) is not valid, as we have now two bodies with their own frequency. The linear approach is only valid if the line is stiff at all times.

2.3. Differences to Linear Generator

As a conclusion of this section, three differences between a rotational direct-driven generator compared to a linear one should be pointed out:

- The damping is increased by factor $(r_d/r_l)^2$ for the rotational direct-driven generator, less magnets/coils are needed for the same damping.
- If $r_c > r_l$, the inertia of the rotatory PTO can be much higher with the same weight. The eigenfrequency decreases with the inertia.
- The stroke length of the rotational PTO is not directly limited by the generator height.
- For a rotatory motor a good bearing (e.g., roller bearing) is much easier to design than for a translatory generator. On the other hand, the force acting on the rotatory bearing is much higher than on a linear generator bearing. Furthermore a winch based rotatory generator has friction due to the rope unwinding.

3. Theory of Wave Body Interactions

In this paper, linear potential theory is used to describe the wave-body interaction, assuming an irrotational, incompressible fluid and non-steep waves. This assumption is a reasonable approximation for the non-steep, operational waves considered here [33]. Using potential flow, a velocity potential ϕ can be defined fulfilling the Laplace equation. The free kinematic and dynamic free surface boundary condition are:

$$\frac{\partial^2 \phi}{\partial t^2} + g \frac{\partial \phi}{\partial z}\bigg|_{z=0} = 0\,, \tag{12}$$

$$\eta = -\frac{1}{g} \frac{\partial \phi}{\partial t}\bigg|_{z=0}\,, \tag{13}$$

where η is the surface elevation. The sea bed boundary condition is:

$$\left[\frac{\partial \phi}{\partial z}\right]_{z=-h} = 0\,, \tag{14}$$

with h being the height of the water surface above the sea bed.

The interaction between a buoy and a wave can be described with three waves: The excitation wave induces a force on the body, the movement of the buoy causes a radiated wave and the presence of the buoy's shape is an obstacle for the incoming wave, resulting in a scattered wave.

The velocity potential is the sum of the undisturbed incident φ_0, the scattered φ_S and the radiated φ_R part. The latter can be calculated from the motion of the buoy:

$$\varphi_R = i\omega \sum_{j=1}^{6} x_{bj}\varphi_j\,, \tag{15}$$

where x_{bj} is the motion of the buoy in coordinate j and ω is the frequency of the wave. Integrating the velocity potential over the wetted surface S results in the excitation force acting on the buoy:

$$F_{e,j} = i\omega\rho \iint_S (\phi_0 + \phi_S) n_j dS\,, \tag{16}$$

with n_j being the normal vector in direction j [33,34].

4. Physical Experiments

4.1. Physical Model Set-up

The physical model presented in Section 2 is used, with a 40-mm wide and 2-mm thick aluminium discs (AL1050). Its weight is 0.660 kg, which is equivalent to a full scale linear translator with 47.5 t inertia. To consider also the inertia of the IMU and the bolts holding it, the rounded value 48 t is used. The weight of the PTO m_w refers to a full scale weight of 5 tonnes. Two discs can be mounted on the hub allowing the disc inertia to be 48 or 96 t. A overview over all relevant parameters can be found in Table 1.

The damping was examined with a "free fall" test, where only the force of the weight and no buoy as counter force is acting on the system. The damping coefficient can then be calculated from the steady state velocity and the weight.

Figure 3 shows the damping in this steady state condition. It is clearly visible that the damping is not constant over a period, the deviation from the mean velocity correlates well with the disc position. This may be explained that despite high-precision manufacturing methods, the disc is not completely plane, which results in a slight changing of the distance between disc and magnets. However, the divergence is within $\pm 5\%$ and thus relatively small.

Table 1. Parameters of the scale model and their Froude-scaled full scale equivalence.

Parameter	Model Scale Value	Full Scale Value
disc radius (r_s)	0.2 m	2 m
attachment radius (r_w and r_l)	10 mm	0.1 m
Mass weight (m_w)	5 kg	5000 kg
Mass buoy (m_b)	5 kg	5000 kg
Inertia disc (J)	48 kg	48,000 kg
PTO damping (d_{PTO})	312 Nm/s	100 kNm/s
Sea state duration	6.5 min	20 min

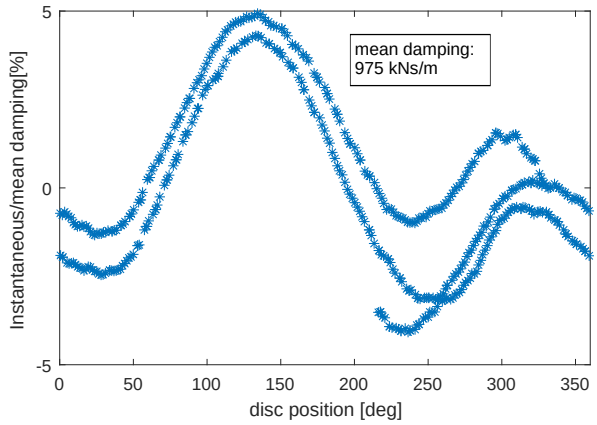

Figure 3. Instantaneous damping related to the mean damping, plotted over the disc position. The calculation is based on the disc rotational velocity after reaching constant velocity while a force of 12.5 N (model scale) is acting on the line. Mean damping is full scale equivalent. Graph shows one test with 2.25 revolutions.

The test was redone without damping and different weights (0.115, 0.5, 1 and 2 kg, model scale) to verify the inertia of the disc and measure the friction in the system, see Figure 4. The measured acceleration in steady state was compared to the theoretically value. From the graph the friction was estimated to about 0.6 N (model-scale). The heavy oscillation for the 0.5 kg and 0.115 kg cases can be explained with the weight of the IMU, that makes the disc slightly unbalanced. However this effect is very small.

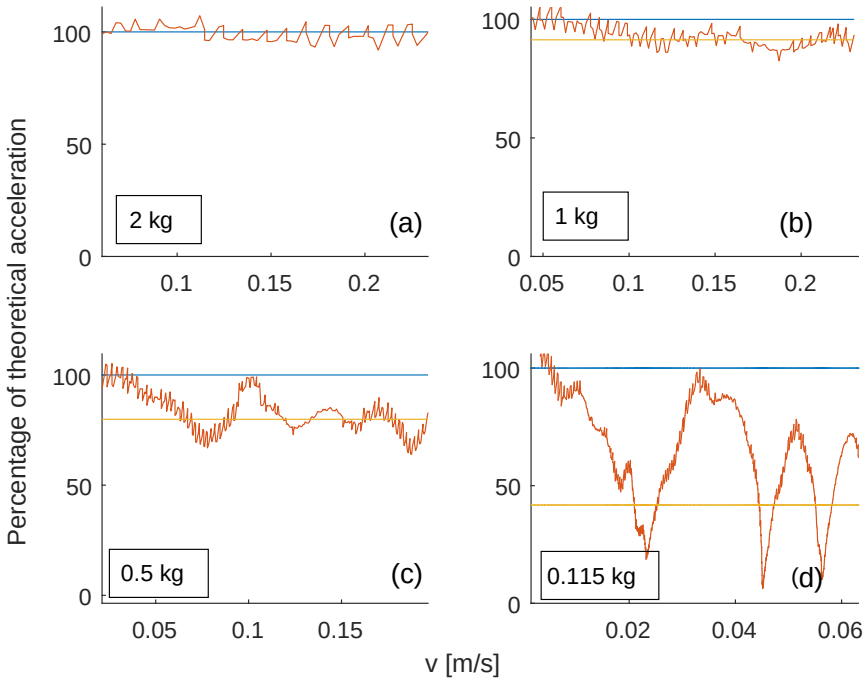

Figure 4. Acceleration measured and low pass filtered (orange) in relation to the theoretical acceleration (100%, blue line). The yellow line represents the value the measured acceleration tends to. Values are directly measured from the scale model.

The relation between clamp gap and damping from Equation (1) was verified once again with a "falling" weight, by changing the air gap of the vice (measured in lever turns). The results of this test are compared to Equation (1) in Figure 5. If v is constant, the damping is directly proportional to the

magnetic flux B. In the figure the proportionality constant is chosen so that both graphs agree at clamp position '0'. The buoy is connected to the PTO with a line guided by a pulley system. The pulleys have a ball bearing and rotate nearly frictionless. From the PTO the line is guided over the gantry on which the PTO is placed, from there down to the floor of the wave basin and then to the buoy. The stiffness of the line between weight and buoy is estimated to 133.33 kN/m. The low stiffness is mostly caused by the knots and the aluminium profile the pulleys are mounted, rather by the line itself.

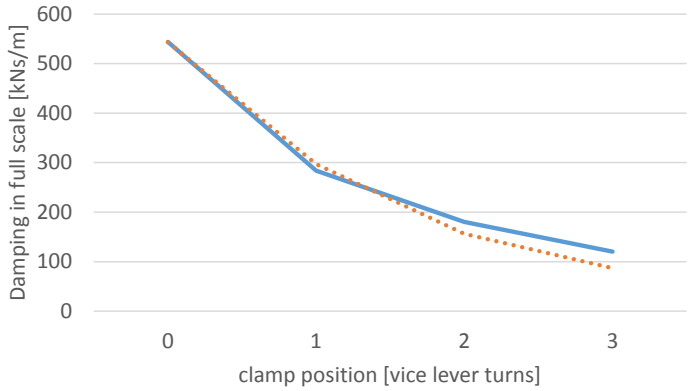

Figure 5. Measured damping of the PTO (blue) in relation to the gap width, measured in turns of the vice knob. The dotted line shows the trend of the magnetic flux according to Equation (1). The curve is scaled so that it matches with the measurement for the zero clamp position.

4.2. Wave Tank Tests

The wave tank tests were performed in the Ocean Basin in the COAST Laboratory at the University of Plymouth, a photo and sketch of the set-up can be found in Figure 6. The tests were conducted at a full-scale equivalent depth of 25 m.

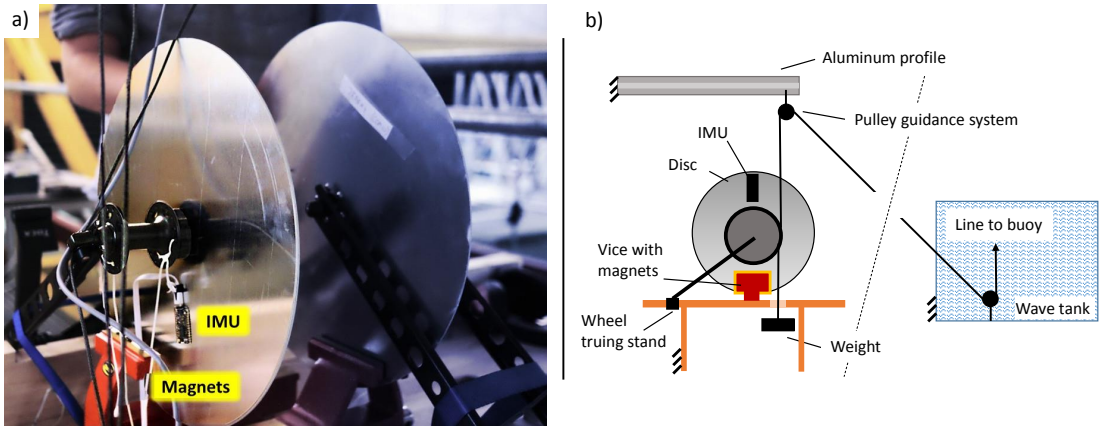

Figure 6. (**a**) Photo of the physical scale model; (**b**) Schematic of the set-up during the scale model testing in the wave tank.

The full-scale equivalent buoy measures 5 m in diameter and weights 5000 kg and can be in good agreement described as ellipsoidal shaped.

The eight 20 min long Brettschneider sea states performed in the tank tests form a 4×2 power matrix which consists of four wave periods ranging from $T_e = 3.5$ s to 9.5 s and two significant wave heights, $H_s = 0.75$ m and 1.75 m. Two matrices were performed for a PTO equipped with one disc and two discs respectively, leading to a total inertia of 53 t and 101 t.

5. Numerical Simulations

5.1. Numerical Model

The WEC was modelled as a two body system connected with the line force F_l. The total force on the buoy is:

$$F_B = F_e + F_r + F_h + F_{Gb} + F_l + m_b\ddot{x}(t): \tag{17}$$

The excitation force F_e is calculated as a convolution between the impulse response function $h_e(t)$ of the buoy and the incident wave elevation $\eta(t)$. The damping force F_r due to the radiated wave is obtained in a similar manner by convolution $h(t)$ with the velocity $\dot{x}(t)$. The hydrostatic force F_h of the buoy is the product of the buoyancy b_b at equilibrium and $x(t)$ the position of the buoy below the surface (draft). Furthermore the gravity force F_{Gb} is the product of the mass of the buoy m_b and the gravity acceleration.

The PTO is modelled as a linear translator with additional inertia, implying that $r_w = r_d = r_l$. The generator provides an ideal damping, so Equation (6) becomes:

$$F_{PTO}(t) = d_{PTO}\dot{y}(t) + M\ddot{y}(t) + F_l(t) + m_w g\,, \tag{18}$$

with y being the position of the weight. With its non-linear behaviour the line force is simulated with the following equation:

$$F_l(t) = \begin{cases} c_l(x(t) - y(t)) + d_l(\dot{x}(t) - \dot{y}(t)) & , x > y \\ 0 & , \text{else} \end{cases}\,, \tag{19}$$

with c_l and d_l being the line stiffness and damping. They were chosen to mimic an ideal line and at the same time avoid numerical oscillation. To obtain the hydrodynamic parameters the commercial software WAMIT [34] (based on the boundary elements method) was used. The hydrodynamic parameters were calculated for wave periods up to 16 s, with a resolution of 0.1 s and then inverse-Fourier transformed into time-domain. As solver a delayed-differential-equation solver (DDE) with 0.1 ms fixed step size is used. A flow chart of the solver can be found in Figure 7.

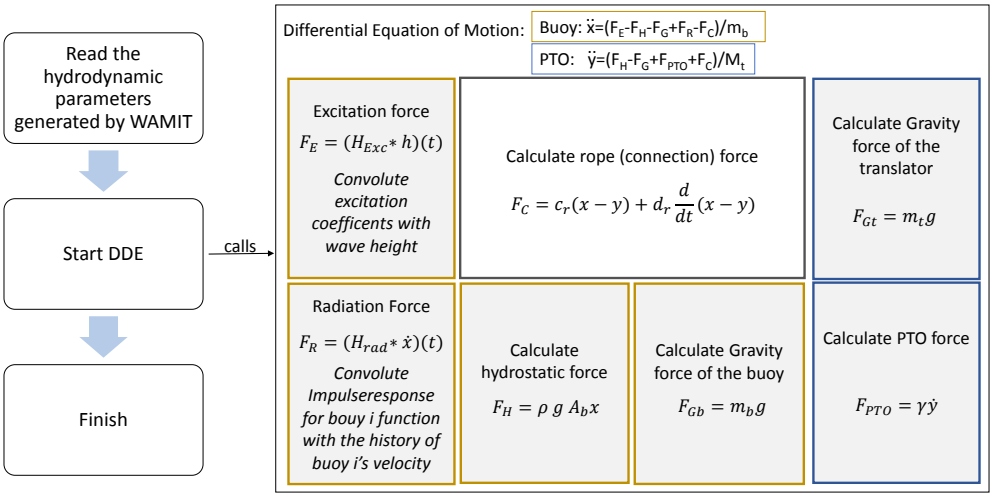

Figure 7. Diagram of the numerical simulation.

5.2. Parameters

Similar to the wave tank tests, a buoy measuring 5 m in diameter, but with a cylindrical shape, and a weight of 5000 kg is used. For different rotational inertiae mass (J) and generator damping

coefficients (d_{PTO}), the performance of the PTO for a power matrix with wave energy periods ranging from $T_e = 3.5$ s to 9.5 s and significant wave height between $H_s = 0.75$ s and $H_s = 3.75$ s were tested. For $J = 0$, the rotational PTO and the linear PTO are identical, and therefore this configuration is used as reference. As in the wave tank test, each sea state had a duration of 20 min.

6. Results and Discussion

The simulated power matrix can be found in Figure 8. For each inertia, a matrix with a low generator damping of 75 kNs/m and a moderate damping of 125 kNs/m is simulated. The power output of the high-inertia PTOs were set in relation to a PTO with $M = m_w$, which can be seen as a linear generator. Figure 9 plots the velocity of the PTO with $M = 45$ t and $M = 120$ t.

M=120 t, m=5 t, d=75 kNs/m

T [s] / Hs [m]	3.5	5.5	7.5	9.5
0.75	146%	239%	211%	162%
1.75	87%	147%	167%	159%
2.75	61%	111%	137%	143%
3.75		95%	124%	135%

M=45 t, m=5 t, d=75 kNs/m

Hs [m]	3.5	5.5	7.5	9.5
0.75	186%	139%	110%	95%
1.75	167%	139%	111%	95%
2.75	142%	138%	118%	101%
3.75		136%	124%	109%

M=120 t, m=5 t, d=125 kNs/m

T [s] / Hs [m]	3.5	5.5	7.5	9.5
0.75	124%	193%	197%	177%
1.75	86%	133%	157%	163%
2.75	65%	104%	128%	141%
3.75		90%	113%	109%

M=45 t, m=5 t, d=125 kNs/m

Hs [m]	3.5	5.5	7.5	9.5
0.75	142%	139%	130%	123%
1.75	130%	130%	126%	122%
2.75	114%	120%	120%	119%
3.75		114%	116%	109%

Color key: 0% 20% 40% 60% 80% 100% 120% 140% 160% 180% 200%

Reference: M=m=5 t mass and d=125kNs/m

Figure 8. Matrix of power output for two direct-driven PTOs with different inertia, but the same weight, calculated by the numerical simulation and compared to a generator with $M = m_w$, so a linear generator.

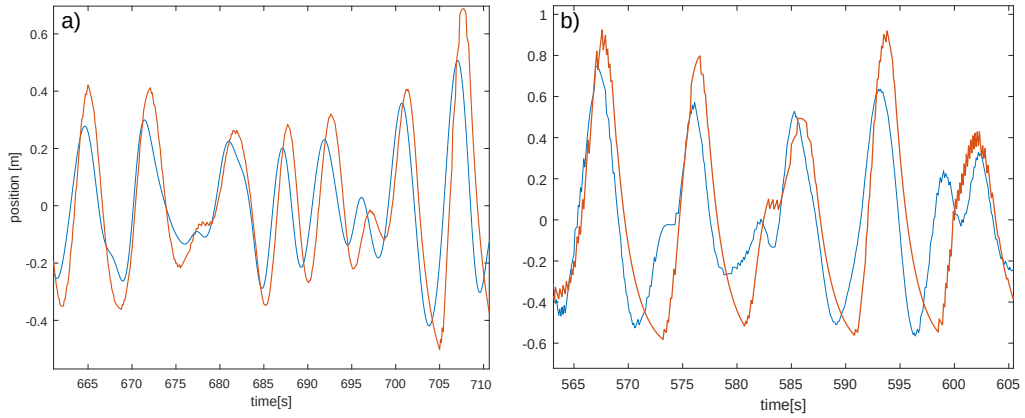

Figure 9. Position of the translator in the numerical simulation for Ts = 7.5 s and Hs = 0.75 m (**a**), and Hs = 1.75 m (**b**). The thin blue curve is from the PTO with low inertia (45 t), the thick orange curve with high inertia (120 t). The damping was set to 75 kNs/m. All values scaled to full scale equivalents.

Figure 10 shows the power matrices performed in the wave tank: The first matrix shows the absorbed power of the low inertia, the second matrix of the high inertia PTO; the third matrix shows the realtion between the low and high inertia PTO. The generator damping was fixed for all sea states to 100 kNs/m. The motion for both PTO in two sea states is plotted in Figure 11.

To compare the numerical simulation and physical wave tank test in Figure 12, the numerical simulation was executed for the $M = 53$ kg case with a damping of $d = 100$ kNs/m. For the line stiffness, firstly the nearly ideal parameter as used in the simulation of the power matrix are used and then the estimated parameter of the real line.

Power [W], M=65 t, m=5 t, d=100 kNs/m

Hs [m] \ Ts [s]	3.5	5.5	7.5	9.5
0.75	223	626	800	756
1.75	2289	4095	5311	5036

Power [W], M=125 t, m=5 t, d=100 kNs/m

Hs [m] \ Ts [s]	3.5	5.5	7.5	9.5
0.75	155	639	919	915
1.75	1336	2768	4416	4806

Power(M=125 t)/Power(M=65t)

Hs [m] \ Ts [s]	3.5	5.5	7.5	9.5
0.75	69%	102%	115%	121%
1.75	58%	68%	83%	95%

Color key:

0
1000
2000
3000
4000
5000
6000

50%
80%
110%
140%

Figure 10. Matrix of generated power ($d_{PTO}v^2$) for two direct-driven PTOs with different inertia, but same weight, results of the wave tank test.

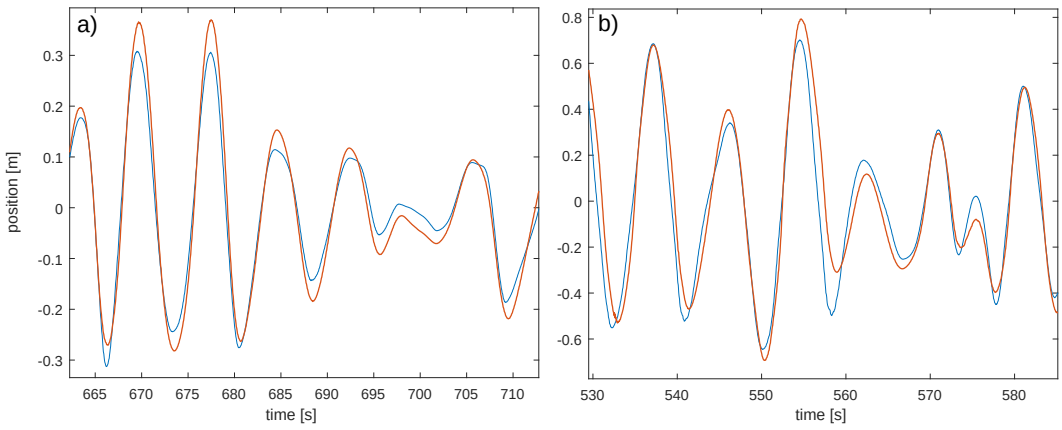

Figure 11. Position of the translator in the wave tank tests for Ts = 7.5 s and Hs = 0.75 m (**a**), and Hs = 1.75 m (**b**). The thin blue curve is from the PTO with low inertia (53 t), the thick orange curve with high inertia (101 t). The damping was set to 100 kNs/m. All values scaled to full scale equivalents.

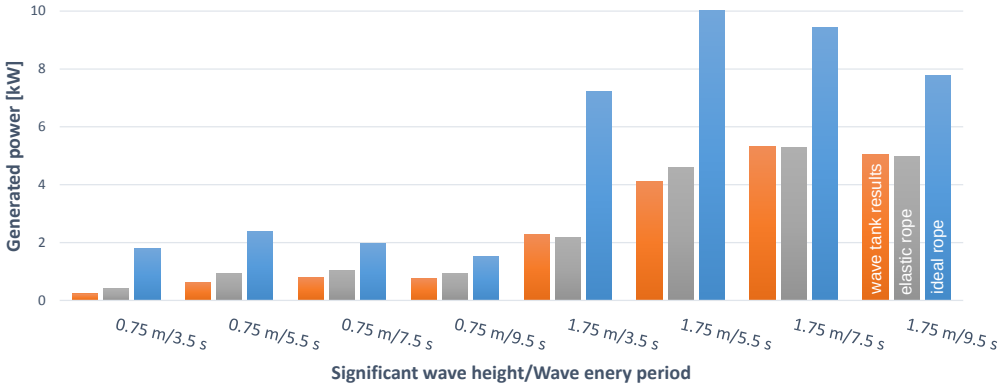

Figure 12. Comparison of the generated power in the physical wave tank tests (**orange**), the numerical simulation using a medium stiff line with $c_l = 133$ kN/m and $d_l = 10$ kN/m (**grey**) and the numerical simulation using an ideal stiff line with $c_l = 4$ GN/m and $d_l = 1$ kN/m (**blue**). The inertia was set to $M = 53$ kg.

6.1. Numerical Simulations

For nearly all sea states (80–100%) the higher inertia is beneficial (see Figure 8). Only for a few sea states with short periods and high waves, the linear reference PTO absorbs significantly more power. The predicted power increase when shifting the natural frequency towards the wave frequency, good to see for low sea states, with the power absorption increasing up to +139%. Outside the peak frequency the additional power is much less.

In the linear equation used in section 3, the wave height had no influence on the absorbed power. However, in the simulation the higher inertia PTOs advantage drops significantly when increasing the wave height. Here the non-linear effect of the line may play a role, limiting the downward speed of the PTO to $v = m_w g / d_{PTO}$. Figure 9 correspondents with this observation: For $H_s = 0.75$ m both PTOs show a smooth curve; the high inertia PTO shows a nearly ideal sinusoidal shape, indicating a good frequency match. The high inertia PTO reaches a faster speed in the downwards movement than the low inertia PTO. For $H_s = 1.75$ m, only the low inertia has a continuous movement, while the high inertia PTO has a sharp knick at the bottom position, caused by the frequency mismatch when the translator weight is still in the downwards movement, but the buoy, following the wave, is already moving upwards. The maximal downwards speed in this sea state is the same for both PTOs, it is limited by the generator damping and weight. A higher generator weight could reduce the negative effects on the absorbed power in higher sea states.

Focusing on the damping, the difference in the resonators bandwidth (characterized by the Q-factor) can be seen: The low damping leads to a higher Q-factor, and so to a higher peak power. While the peak power for the higher damping is smaller, the decrease in power off the resonance centre is smaller.

6.2. Numerical Simulations and Physical Tests

The results of the physical wave tank tests shown in Figure 8 are slightly different: For the low amplitude waves and long wave periods, the high inertia PTO has an advantage over the low inertia PTO. For short periods the low inertia PTO generates more power. However, for $H_s = 1.75$ m waves, the low inertia is beneficial for all tested periods. The difference is getting smaller as higher the wave period is, and for wave energy periods higher than 9.5 s the high inertia PTO may absorb more power. But comparing to the simulation power matrix in Figure 8, the higher inertia should perform better from $T_e = 5.5$ s upwards.

This may be explained with the ideal stiff line in the simulation. Figure 12 shows the influence of the line stiffness: While using the ideal line, the numerical simulation absorbs approximately 2 times, in low sea states up to 10 times of the power of the physical tests. While reducing the stiffness of the line, the power rapidly plunges very close to the wave tank test result. Also the peak period changes towards the higher wave energy periods. The line reduced stiffness used was with 133 kN/m very low. We assume that the low stiffness results primary from the knots connecting the different part together and that the line stiffness itself plays a secondary role. The low line stiffness may therefore only be valid for small displacements.

The differences between numerical simulations with the non-ideal line and physical wave tank tests are very small. For the low waves, the predicted power from the simulation is slightly higher, what might be a result of the friction in the system. For the 1.75 m waves, the agreement is very good, but the peak frequency for the simulation seems to be between 5.5 s and 7.5 s, while for the physical tests it seems to be between 7.5 s and 9.5 s. Differences may be caused by reflections in the wave tank, limits of the linear potential wave theory, the heave only simplification or inaccuracies of the PTO system. The cylindrical shape of the buoy in the simulation and the ellipsoidal shape in the wave tank test have nearly no influence on the results: In the numerical model the buoyancy stiffness is linearised at the steady state draft, where it is the same for both shapes.

Similar tests comparing a physical with a numerical point absorber WEC model were performed by [11]. The physical scale model uses a motor to mimic the PTO and is designed without using

connecting lines. The measured data from the physical tests agrees very well with the model data, and no line elasticity has to be considered. However, while the motor allows a wide range of control strategies to be simulated, it results in a clearly visible noise in the passive damping mode especially for high and short period waves.

The time series of the physical experiments matches in general the observation from the numerical simulation: The high inertia PTO matches the wave frequency very well in the low amplitude waves, what can be seen in the higher peaks in Figure 11, but for the low inertia, the period is too high to catch all peaks.

In direct comparison with the numerical results of Figure 9, the experimental curves look smoother. The sharp knick as seen for the high inertia PTO in the high wave in the simulation does not exist in the experimental results. Here the line elasticity may have smoothed the results.

6.3. Overall

Despite the differences in simulation and physical test, mostly caused by the line stiffness, the overall characteristics are the same: The peak frequency for a PTO increases with its inertia, and the benefit from the frequency matching decreases with the wave height. With the damping the resonance bandwidth can be adjusted and so the ratio between absorbed peak power and power off the resonance centre. This is especially important as an uncontrolled PTO can not adjust its frequency.

The experiments showed that tuning the undamped eigenfrequency of the PTO towards the energy period of the sea state is not always beneficial. While in sea states with low wave height sea states, the natural frequency from the linear estimation agrees well with the real behaviour of the PTO, in higher and steeper waves it leads to a slack line, thus reducing the benefit of the frequency tuning. On the other side, compared to a traditional low inertia PTO, the absorbed power is for nearly all sea states in the power matrix in Figure 8 much higher. Control strategies, like latching or complex conjugate control, rely on a PTO with high frequency and may provide better results for a wider range of sea states, due to their ability to adapt to the sea state. But controllable PTO designs require additional electrical or mechanical mechanism, and suitable controller for real sea states are still a topic of ongoing research. For many wave climates, a well tuned, non adjustable frequency may be good enough. When designing the WEC converter to match a specific sea states, the energy adsorption for this sea state may increase significantly, however, on the other side, it will get out of tune for sea states far away. This can be used to automatically detune the device in storm conditions.

The results of the added inertia from Figures 8 and 10 agree well with the effect of an additional submerged added mass sphere in [8], where the absorbed power with the additional inertia sphere is increased up to the factor of 3 compared to the linear generator without the sphere. Even though the generator design was similar to the one used in this paper, the specific parametrization and sea states were different, so that the values can not be compared directly. In [22], while analysing the influence of inertia on a cylindrical bottom-hinged WEC, the absorbed power of the increased inertia WEC correlates with the wave period. However, it also increases if the wave amplitude gets higher, which opposes the finding in this paper and is a good example of the fact that the characteristics between different WEC types alter.

7. Conclusions

In this paper a new design of a physical model PTO with constant damping was presented, showing a simple and accurate way to get low friction PTO with a nearly ideal velocity dependent force.

The alternating rotatory design combines the simplicity of a direct-driven generator by having no gearbox, beside a disc, with the advantages of a rotational system such as a decoupling of stroke and generator length.

The additional inertia allows to design the device for specific sea states and the PTO damping can be used to adjust the degree of specialisation. This can be used to build a simple control-free WEC,

tuned for the most significant sea state in a certain wave climate. Away from this sea state, for example in harsh, stormy conditions, the WEC will automatically detune.

In numerical simulations with an ideal connection line between buoy and PTO, the additional inertia provided up to 239% of the power of a similar generator where the inertia is equivalent to the weights (direct-driven linear generator). For the parametrisation with the smallest Q-factor 80% of the tested sea states still had an increase in power absorption compared to a linear generator. However, at lower wave energy periods and higher waves heights the advantage in power absorption of the high inertia PTO compared to the linear generator gets smaller.

The findings of the numerical simulation are confirmed in wave tank tests. Here, the stiffness of the line showed a big influence on the system. A low line stiffness decreases the absorbed power and increased the peak wave period.

Due to the simple design and the the good performance without control, alternating rotatory generators might also be an interesting option for full-scale devices operating in wave climates with small energy spectrum bandwidth.

Further improvements of the physical model could include a replacement of the permanent magnets with electro magnets as used in [27] which allow a quick and reliable change of the damping as well as adjustable damping control strategies.

Supplementary Materials: The position and velocity data of the physical scale tests are available online at http://www.mdpi.com/1996-1073/11/9/2332/s1.

Author Contributions: The general conceptualization and methodology were done by S.T. The conceptualization and methodology for the wave tank test were mostly done by S.T. and M.G. (Marianna Giassi) with help from M.G. (Malin Göteman), J.E., M.H. and E.R. Project administration, including supervision, was done by M.G. (Malin Göteman), J.E., M.H., E.R. and J.I., M.G. (Malin Göteman), J.E. and J.I. were furthermore responsible for the funding acquisition.

Funding: The authors want to thank the Swedish Energy Agency (project number 40421-1), the Swedish Research Council (VR, grant number 2015-04657) for funding this research and the Åforsk Foundation. This work was supported by Stand Up for Energy.

Acknowledgments: This paper would not exist in this form without the help of Tom Tosdevin who helped a lot preparing the physical PTO and adjusting the damping. With their fast and uncomplicated help the team of Plymouth University's coast lab, especially Kieran Monk, Alastair Reynolds, Hannah Poulson, Gregory Nash and Andy Oxenham played an important part in securing that the PTO was finished in time.

Conflicts of Interest: The authors declare no conflict of interest.

Abbreviations

The following abbreviations are used in this manuscript:

WEC	Wave energy converter
PTO	Power take-off
IMU	Inertia measurement unit
WAMIT	WaveAnalysisMIT; Wave interaction analysing tool
COAST laboratory	Coastal, ocean and sediment transport laboratory; Facility at the University of Plymouth containing the wave tank
Q-factor	quality factor
DDE	Delayed differential equation
g	gravity acceleration

References

1. Clément, A.; McCullen, P.; Falcão, A.; Fiorentino, A.; Gardner, F.; Hammarlund, K.; Lemonis, G.; Lewis, T.; Nielsen, K.; Petroncini, S.; et al. Wave energy in Europe: Current status and perspectives. *Renew. Sustain. Energy Rev.* **2002**, *6*, 405–431. [CrossRef]

2. Allan, G.; Gilmartin, M.; McGregor, P.; Swales, K. Levelised costs of wave and tidal energy in the UK: Cost competitiveness and the importance of "banded" renewables obligation certificates. *Energy Policy* **2011**, *39*, 23–39. [CrossRef]
3. Ocean Energy: Cost of Energy and Cost Reduction Opportunities. Available online: https://energiatalgud.ee/img_auth.php/1/10/SI_OCEAN._Ocean_Energy_-_Cost_of_Energy_and_Cost_Reduction._2013.pdf (accessed on 13 August 2018).
4. Lejerskog, E.; Strömstedt, E.; Savin, A.; Boström, C.; Leijon, M. Study of the operation characteristics of a point absorbing direct driven permanent magnet linear generator deployed in the Baltic Sea. *IET Renew. Power Gener.* **2016**, *10*, 1204–1210. [CrossRef]
5. Wang, W.; Wu, M.; Palm, J.; Eskilsson, C. Estimation of numerical uncertainty in computational fluid dynamics simulations of a passively controlled wave energy converter. *Proc. Inst. Mech. Eng. Part M J. Eng. Marit. Environ.* **2018**, *232*, 71–84. [CrossRef]
6. Valério, D.; Beirão, P.; da Costa, J.S. Optimisation of wave energy extraction with the Archimedes Wave Swing. *Ocean Eng.* **2007**, *34*, 2330–2344. [CrossRef]
7. Todalshaug, J.; Falnes, J.; Moan, T. A comparison of selected strategies for adaptive control of wave energy converters. *J. Offshore Mech. Arct. Eng.* **2011**, *133*, 031101.
8. Engström, J.; Kurupath, V.; Isberg, J.; Leijon, M. A resonant two body system for a point absorbing wave energy converter with direct-driven linear generator. *J. Appl. Phys.* **2011**, *110*, 124904, [CrossRef]
9. Yurchenko, D.; Alevras, P. Dynamics of the N-pendulum and its application to a wave energy converter concept. *Int. J. Dyn. Control* **2013**, *1*, 290–299. [CrossRef]
10. Göteman, M.; Engström, J.; Eriksson, M.; Leijon, M.; Hann, M.; Ransley, E.; Greaves, D. Wave Loads on a Point-Absorbing Wave Energy Device in Extreme Waves. *J. Ocean Wind Energy* **2015**, *2*, 176–181. [CrossRef]
11. Beatty, S.; Ferri, F.; Bocking, B.; Kofoed, J.; Buckham, B. Power Take-Off Simulation for Scale Model Testing of Wave Energy Converters. *Energies* **2017**, *10*, 973. [CrossRef]
12. Thomas, S.; Giassi, M.; Göteman, M.; Eriksson, M.; Isberg, J.; Engström, J. Optimal Constant Damping Control of a Point Absorber with Linear Generator In Different Sea States: Comparision of Simulation and Scale Test. In Proceedings of the 12th European Wave and Tidal Energy Conference, Cork, Ireland, 27 August 2017.
13. Ewart, L.B.; Thies, P.R.; Stratford, T.; Barltrop, N. Optimising structural loading and power production for floating wave energy converter. In Proceedings of the 12th European Wave and Tidal Energy Conference, Cork, Ireland, 27 August 2017.
14. Bosma, B.; Lewis, T.; Brekken, T.; von Jouanne, A. Wave Tank Testing and Model Validation of an Autonomous Wave Energy Converter. *Energies* **2015**, *8*, 8857–8872. [CrossRef]
15. Têtu, A.; Power Take-Off Systems for WECs. In *Handbook of Ocean Wave Energy*; Pecher, A., Kofoed, J.P., Eds.; Springer International Publishing: Cham, Switzerland, 2017; pp. 203–220.
16. Al-Habaibeh, A.; Su, D.; McCague, J.; Knight, A. An innovative approach for energy generation from waves. *Energy Convers. Manag.* **2010**, *51*, 1664–1668. [CrossRef]
17. Lok, K.; Stallard, T.; Stansby, P.; Jenkins, N. Optimisation of a clutch-rectified power take off system for a heaving wave energy device in irregular waves with experimental comparison. *Int. J. Mar. Energy* **2014**, *8*, 1–16. [CrossRef]
18. Polinder, H.; van der Pijl, F.F.A.; de Vilder, G.J.; Tavner, P.J. Comparison of direct-drive and geared generator concepts for wind turbines. *IEEE Trans. Energy Convers.* **2006**, *21*, 725–733. [CrossRef]
19. Cheng, M.; Zhu, Y. The state of the art of wind energy conversion systems and technologies: A review. *Energy Convers. Manag.* **2014**, *88*, 332–347. [CrossRef]
20. Rhinefrank, K.; Schacher, A.; Prudell, J.; Hammagren, E.; von Jouanne, A.; Brekken, T. Scaled development of a novel Wave Energy Converter through wave tank to utility-scale laboratory testing. In Proceedings of the 2015 IEEE Power Energy Society General Meeting, Denver, CO, USA, 26–30 July 2015; pp. 1–5.
21. Sjolte, J.; Tjensvoll, G.; Molinas, M. Power Collection from Wave Energy Farms. *Appl. Sci.* **2013**, *3*, 420–436. [CrossRef]
22. Flocard, F.; Finnigan, T. Increasing power capture of a wave energy device by inertia adjustment. *Appl. Ocean Res.* **2012**, *34*, 126–134. [CrossRef]
23. Sheng, W.; Lewis, T. Energy Conversion: A Comparison of Fix- and Self-Referenced Wave Energy Converters. *Energies* **2016**, *9*, 1056. [CrossRef]

24. Sidenmark, M.; Josefsson, A.; Berghuvud, A.; Broman, G. The Ocean Harvester: Modelling, Simulation & Experimental Validation. In Proceedings of the 8th European Wave and Tidal Energy Conference, Uppsala, Sweden, 7–10 September 2009.
25. Larsson, K. Investigation of a Wave Energy Converter with a Flywheel and a Corresponding Generator Design. Master's Thesis, Chalmers University of Technology, Goteborg, Sweden, June 2012.
26. Castellucci, V.; Eriksson, M.; Waters, R. Impact of Tidal Level Variations on Wave Energy Absorption at Wave Hub. *Energies* **2016**, *9*, 843. [CrossRef]
27. Lopes, M.; Henriques, J.; Lopes, M.; Gato, L.; Dente, A. Design of a non-linear power take-off simulator for model testing of rotating wave energy devices. In Proceedings of the 8th European Wave and Tidal Energy Conference, Uppsala, Sweden, 7–10 September 2009.
28. Payne, G.; Taylor, J.; Parkin, P.; Salter, S. Numerical modelling of the sloped IPS buoy wave energy converter. In Proceedings of the International Offshore and Polar Engineering Conference, Sapporo, Japan, 10–15 June 2006.
29. Yu, Y.H.; Lawson, M.; Li, Y.; Previsic, M.; Epler, J.; Lou, J. *Experimental Wave Tank Test for Reference Model 3 Floating- Point Absorber Wave Energy Converter Project*; Technical Report; National Renewable Energy Laboratory: Golden, CO, USA, 2015.
30. Mercadé Ruiz, P.; Ferri, F.; Kofoed, J.P. Experimental Validation of a Wave Energy Converter Array Hydrodynamics Tool. *Sustainability* **2017**, *9*, 115. [CrossRef]
31. Lejerskog, E.; Gravråkmo, H.; Savin, A.; Strömstedt, E.; Tyrberg, S.; Haikonen, K.; Krishna, R.; Boström, C.; Rahm, M.; Ekström, R.; et al. Lysekil Research Site, Sweden: A status update. In Proceedings of the 9th European Wave and Tidal Energy Conference, Southampton, UK, 5–9 September 2011.
32. Ekström, R.; Ekergård, B.; Leijon, M. Electrical damping of linear generators for wave energy converters—A review. *Renew. Sustain. Energy Rev.* **2015**, *42*, 116–128. [CrossRef]
33. Falnes, J. *Ocean Waves and Oscillating Systems: Linear Interactions Including Wave-Energy Extraction*; Cambridge University Press: Cambridge, UK, 2002.
34. WAMIT User Manual Version 7.0. Available online: http://www.engr.mun.ca/~bveitch/courses/8000/software/wamit/wamit.pdf (accessed on 13 August 2018).